Research Paper
Computational Methods for Differential Equations
http://cmde.tabrizu.ac.ir
Vol. *, No. *, *, pp. 1-13
DOI:10.22034/cmde.2025.66849.3163

Computational analysis of micromagnetorotation within micropolar flow through implementation in FreeFEM++

Ejaz Haider Awan and Muhammad Sabeel Khan*
Department of Mathematics, Capital University of Science and Technology, 44000 Islamabad, Pakistan.

Abstract

In this paper, a novel micromagnetorotation boundary layer model is presented and analysed with its physical significance on the thermal micropolar flow by computations using finite element method in FreeFEM++. Firstly, the theory of magnetorotation is taken into account within the framework of micropolar continuum to develop an ODE model. Secondly, the developed model is then implemented through open-source code for the first time in the literature. It is worth mentioning that FreeFEM++ does not have this capability inbuilt to handle one-dimensional simulations. In this study we successfully implemented and integrated the presented one-dimensional ODE model in FreeFEM++. Thermal flow characteristics are revisited in the presence of micromagnetorotation effects. This study is first of its kind since the energy equation incorporated with microcmagnetorotation effect is calculated using concepts of vector-tensor calculus. The results are shown against physical parameters of interest, i.e., the skin-friction coefficient and Nusselt number with micromagnetorotation effect. Moreover, thermal and hydrodynamic boundary layer profiles are also calculated with micromagnetorotation effects under different physical settings. Some interesting new findings are drawn and discussed in detail. This study finds its applications in the chemical and transport processes that are involved in industrial research such as in bio-engineering and magnetohydrodynamics.

Keywords. Numerical analysis, Finite elements, Boundary layer flow, Micorpolar, Micromagnetorotation.

2010 Mathematics Subject Classification. 35Qxx, 65Lxx, 76Mxx.

1. Introduction

Micropolar fluids within fluid dynamics is a class of fluids that has been studied from many practical applications. Given its extensive applications in numerous scientific and engineering fields, including biological and environmental sciences, the subject has a wide range of potential uses. Furthermore, it is particularly significant in the fields of oceanography, meteorology, blood flow research, bacterial gliding motility, heat and mass transfer, aerodynamics, etc. A significant limitation of the classical hydrodynamic model is its incapacity to represent fluids with microstructure, a key characteristic that render these fluids captivating and indispensable in various applications. Within the context of continuum mechanics, various theories have emerged, encompassing simple microfluids, irregular fluids, micropolar fluids, dipolar fluids, and others. The theory of micropolar fluids [9] is one of the widely recognized theories of fluids with microstructure. A specialized area within fluid dynamics is micropolar magnetohydrodynamics (MHD), which is electrically conducting fluid subjected to magnetic field. This field attracts significant consideration due to its applications in understanding phenomena such as plasma behavior in fusion reactors and the dynamics of space plasma. Some examples of MHD includes anti-cancer therapy, magnetic endoscopic examination and the circulation of blood during surgery.

Sharma et al. [23], explored the heat and mass transfer behavior in MHD micropolar fluids over a stretching sheet incorporating slip effects. Khan et al. [13], numerically calculated the heat and mass transfer of micropolar fluid flow within a rectangular channel. The study incorporates slip flow and convective boundary conditions. Gupta et al. [10],

---

Received: 18 April 2025; Accepted: 14 April 2026.

∗ Corresponding author. Email: muhammad.sabeel@cust.edu.pk.

presented a numerical approach to solve the steady mixed convection electrically conducting micropolar flow over a porous shrinking sheet. The assumptions encompass the notion that the magnetic field change as power functions concerning their distance to the origin. Sheri et al. [25], examined the effects of Hall current and viscous dissipation on the boundary layer analysis of MHD on an unstable, chemically reactive, micropolar rotating fluid flow across a semi-infinite vertical plate. The Boussinesq approximation has been used to generate the pertinent fluid flow equations. The dependence of the surface heat transfer, wall couple stress, skin-friction, and mass transfer rate on the newly discovered thermo-physical parameters is also discussed. To verify the validity and correctness of the finite element code under certain restricting circumstances, it is benchmarked against findings published in the literature. Excellent agreement with published solutions is attained. Shamshuddin et al. [21], discussed how the finite element method can be used to solve a mathematical model for MHD, micropolar fluid flow that is incompressible, dissipative, and chemically reactive; heat and mass transfer from an inclined plate with a heat source/sink through porous media. Using appropriate dimensionless values that can be incorporated into the finite element formulation, the set of governing equations has been reformulated and transformed into dimensionless form under the assumption of a low Reynolds number. A comprehensive analysis of the associated flow structure, heat, and mass transfer has been carried out, and the evolution of multi-physical parameters in these variables is graphically presented in addition to emphasizing the weighted residual scheme's operational characteristics. A finite element computational solution for heat and mass transfer, MHD, incompressible, dissipative, radiative, and chemically reactive micropolar fluid flow, next to an inclined porous plate immersed in a saturated homogenous porous medium, is described by Shamsuddin et al [22]. Effects of heat generation and absorption are included. The radiative heat flux in the energy equation is described using Rosseland's diffusion approximation. Drag effects in the porous media are simulated using a Darcy model. Assuming a low Reynolds number and a low magnetic Reynolds number, the governing transport equations are transformed into a non-dimensional form. Finite element solutions to the boundary value problem are shown using a Galerkin formulation with a weighted residual scheme. Divya et al. [8] conducted a study in which MHD finite element analysis is used to investigate spontaneously convective flow across an exponentially accelerating plate with viscous dissipation numerically. Dimensional partial differential equations are transformed into dimensionally reduced form, and the Galerkin finite element method is used to solve non-dimensional partial differential equations. The main conclusions of this study are as follows: The primary velocity decreases with increasing values of magnetic parameter, Prandtl number, Schmidt number, and Hall parameter, and increases with increasing values of thermal Grashof number, solutal Grashof number, Eckert number, and Dufour number. Abd-Alla et al. [1], analysed heat and mass transfer in MHD peristaltic flow within a micropolar fluids. Yuan et al. [28], studied the nonlinear effects of flows of viscoelastic fluids. Ali et al. [2], discussed the significance of gravity modulation, heat source/sink and MHD on dynamics of micropolar fluid within inclined surface by finite element simulation. Khan et al. in [14, 15], computed magnetic induced flow with higher order continuum using FreeFEM++. Also computationally investigated induced magnetic micropolar flow within a rectangular channel using the same solver. Kumar et al. [19] investigated how applied magnetic or electric fields, heat sink or source, Joule heating, and thermal radiation affected unsteady micropolar flow across a stretched surface. Their research showed that the electric field increases the flow's temperature and velocity in the opposite way to the magnetic field. Sheikholeslami et al. [18] and Lajvardi et al. [17] conducted experimental investigations on the impact of applied magnetic and electric fields on temperature and heat transfer in a ferrofluid. Both studies demonstrated that the magnetic field decreases the temperature of the ferrofluid, while the electric field has the opposite effect. For this purpose, Shizawa and Tanahashi developed a comprehensive magnetohydrodynamic (MHD) micropolar fluid theory incorporating magnetization. This model integrates Eringen's micropolar fluid equations with principles from ferrohydrodynamic and MHD. The determination of a constitutive equation for magnetization involves utilizing the dissipation function and free energy. Aslani et al. [3] studied micropolar MHD flows, a domain often neglecting the MMR effect by considering parallel magnetization and magnetic field vectors.

It's worth mentioning that there is a lack of research investigating the temperature and heat transfer characteristics of MHD micropolar fluids incorporating the micromagnetorotation (MMR) effect [4]. Aslani's research focuses on exploring how MMR affects the heat transfer in a Hartmann micropolar flow [6]. MMR pertain to the impact of magnetization on micropolar fluids when exposed to an external magnetic field. Khan et al. [11], discussed a micropolar continuum model derived from MHD theory. Their work incorporated the effect of MMR in formulating an initial boundary value problem (IBVP) for magneto-micropolar flows. They did not discuss heat transfer with consideration of MMR.

The novel contributions of this study compared to existing research [3, 4, 11] on micropolar MHD flows, lies in two aspects. First, it introduces a novel thermal boundary layer model that integrates the MMR in the heat transfer characteristics within the framework of micropolar continuum theory, which, to the best of our knowledge, has not been reported in the literature. Secondly, the existence of solution is shown in the weaker sense. FreeFEM++ based numerical method is also presented to obtain numerical solution of the proposed boundary value problem. The key advantages of the proposed method based on FreeFEM++ algorithm over other commonly used techniques, such as finite difference, shooting methods, or bvp4c solvers for similar problems is given as follows. The present method is highly flexible in in handling complex coupled boundary layer equations arising from the inclusion of MMR effects together with heat transfer mechanism. It is accurate and numerically stable when dealing with mixed boundary conditions, slip effects, and variable material properties. The capability of handling the same model in higher-dimensional setting with more generalized boundary conditions. compared to low-order methods. To this end, we consider the vector-tensor form of the governing energy equation under the influence of magnetization. Concepts from the vector-tensor calculus is then utilized to calculate the component form of the energy balance equation accounting MMR which afterward is reduced to thermal boundary layer flow model. As an outcome, two new physical parameters arise that describe the underlying physical microstructural effect on the magnetization of the flow characteristics.

The rest of the paper is organized as follows. In Section 2, MMR heat transfer model is described and mathematical model is formulated in the framework of micropolar continuum theory. In Section 3, weak formulation of the problem is stated and the finite element algorithm for computing flow characteristics is presented. In section 4, obtained numerical results are presented and discussed in detail. Finally, conclusions are drawn in Section 5.

2. MMR Heat Transfer Model and Flow Description

This section presents a heat transport model including the MMR effect in three dimensions. In a magnetic micropolar incompressible unsteady flow, let $\overrightarrow{V}$, $\overrightarrow{H}$, $\boldsymbol{W}$, and T stand for the fluid particles' velocity, magnetic field, micro-rotational velocity, and temperature, respectively. The flow, in accordance with the Shizawa and Tanahashi hypothesis [26], is then described by the following set of coupled partial differential equations.

$$\frac{\partial\rho}{\partial t} + \bigtriangledown.(\rho\overrightarrow{V}) = 0, \tag{2.1}$$

$$\rho\frac{d\overrightarrow{V}}{dt} = -\bigtriangledown P + \eta\bigtriangledown^2\overrightarrow{V} + \bigtriangledown\times 2\eta_1(\mathbf{W} - \overrightarrow{\omega}) + J\times\overrightarrow{B} + (\overrightarrow{M}.\bigtriangledown)\overrightarrow{H} + \overrightarrow{M}\times(\bigtriangledown\times\overrightarrow{H}), \tag{2.2}$$

$$I\frac{d\mathbf{W}}{dt} = \gamma\bigtriangledown^2\mathbf{W} - 4\eta_1(\mathbf{W} - \overrightarrow{\omega}) + \overrightarrow{M}\times\overrightarrow{H}, \tag{2.3}$$

$$\begin{aligned}\rho\overline{T}\frac{d\overline{s}}{dt} &= k\bigtriangledown^2\overline{T} + \eta_2(trD^{(v)}) + 2\eta D^{(v)} : D^{(v)} + 4\eta_1(\mathbf{W} - \overrightarrow{\omega})^2\\ &\quad + \alpha tr(\bigtriangledown\mathbf{W}) + \beta(\bigtriangledown\mathbf{W})^T : \bigtriangledown\mathbf{W} + \gamma\bigtriangledown\mathbf{W} : \bigtriangledown\mathbf{W} + \tau\frac{M_0}{\overline{H}}(\mathbf{W}\times\overrightarrow{H})^2,\end{aligned} \tag{2.4}$$

$$\frac{\partial B}{\partial t} = -\bigtriangledown\times\overrightarrow{E}, \tag{2.5}$$

$$\bigtriangledown.\overrightarrow{B} = 0, \tag{2.6}$$

$$\bigtriangledown\times\overrightarrow{H} = J, \tag{2.7}$$

$$J = \sigma(\overrightarrow{E} + v\times\overrightarrow{B}), \tag{2.8}$$

$$\overrightarrow{B} = \mu_0\overrightarrow{H} + \overrightarrow{M}, \tag{2.9}$$

$$\overrightarrow{M} = \frac{M_0(I - \tau\mathbf{W}.\epsilon).\overrightarrow{H}}{\overline{H}}, \tag{2.10}$$

where, in Eqs. (2.1)-(2.10), P, I, M, M_0 and $\overrightarrow{B}$ are the pressure field, identical tensor, magnetization vector, magnetization strength, and magnetic field, respectively. The parameters η, η_1, and γ are the shear stress, vortex and angular viscosity, respectively. Furthermore, ϵ is the Levi-Civita symbol, α, and β, are the spin viscosities. The parameters s, τ, $\overline{T}$, and $\overline{H}$ are the entropy, deformation tensor, relaxation time of magnetization, temperature fields and magnitude of the applied magnetic field vector, respectively. The terms $\overrightarrow{M} \times \overrightarrow{H}$ and $\tau \frac{M_o}{\overline{H}}(\mathbf{W} \times \overrightarrow{H})^2$ are due to MMR, which specifies the influence of magnetization on microrotation. The angular velocity $\overrightarrow{\omega}$ is given by

$$\overrightarrow{w} = \bigtriangledown \times \frac{\overrightarrow{V}}{2}. \tag{2.11}$$

The deformation tensor $\mathbf{D}^{(v)}$ in Eq. (2.4) is defined as

$$\mathbf{D}^{(v)} = \frac{\bigtriangledown \overrightarrow{V} + (\bigtriangledown \overrightarrow{V})^T}{2}. \tag{2.12}$$

Further, assume a low Reynolds number approximation [3], then in a two-dimensional framework (xz-coordinate system), Eqs. (2.1)-(2.10) are stated in component form as

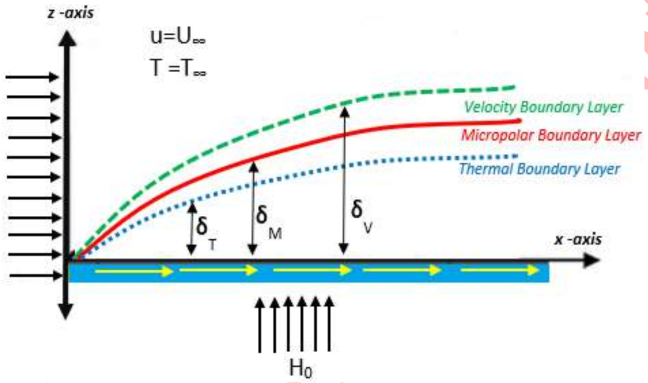

FIGURE 1. Geometry of the problem.

$$\frac{\partial u_1}{\partial x} + \frac{\partial u_3}{\partial z} = 0, \tag{2.13}$$

$$\begin{aligned} \rho\left(u_1\frac{\partial u_1}{\partial x} + u_3\frac{\partial u_1}{\partial z}\right) &= -\frac{\partial p}{\partial x} + J_yB_z + \eta\left(\frac{\partial^2 u_1}{\partial x^2} + \frac{\partial^2 u_1}{\partial z^2}\right) + M_1\frac{\partial H_1}{\partial x} + M_3\frac{\partial H_3}{\partial x} \\ &\quad - 2\eta_1\left(\frac{\partial w_2}{\partial z} - \frac{1}{2}\left(\frac{\partial^2 u_1}{\partial z^2} - \frac{\partial u_3}{\partial z\partial x}\right)\right), \end{aligned} \tag{2.14}$$

$$\begin{aligned} \rho\left(u_1\frac{\partial u_3}{\partial x} + u_3\frac{\partial u_3}{\partial z}\right) &= -\frac{\partial p}{\partial z} + J_yB_x + \eta\left(\frac{\partial^2 u_3}{\partial x^2} + \frac{\partial^2 u_3}{\partial z^2}\right) - M_1\frac{\partial H_1}{\partial z} - M_3\frac{\partial H_3}{\partial z} \\ &\quad + 2\eta_1\left(\frac{\partial w_2}{\partial x} + \frac{1}{2}\left(\frac{\partial^2 u_3}{\partial x^2} - \frac{\partial u_1}{\partial z\partial x}\right)\right), \end{aligned} \tag{2.15}$$

$$u_1\frac{\partial w_2}{\partial x} + u_3\frac{\partial w_2}{\partial z} = \gamma\left(\frac{\partial^2 w_2}{\partial x^2} + \frac{\partial^2 w_2}{\partial z^2}\right) - 2\eta_1\left(2w_2 + \frac{\partial u_1}{\partial z} - \frac{\partial u_3}{\partial x}\right) + M_3H_1 - M_1H_3 \tag{2.16}$$

and

$$\rho\left(u_1\frac{\partial T}{\partial x}+u_3\frac{\partial T}{\partial z}\right)=\kappa\left(\frac{\partial^2 T}{\partial x^2}+\frac{\partial^2 T}{\partial z^2}\right)+\eta_2\left(\frac{\partial u_1}{\partial x}+\frac{\partial u_3}{\partial z}\right)+\eta\left(2\left(\frac{\partial u_1}{\partial x}\right)^2+\left(\frac{\partial u_1}{\partial z}\right)^2\right)$$
$$+4\eta_1\left(w_2-\frac{1}{2}\left(\frac{\partial u_1}{\partial z}\right)\right)^2+\gamma\left(\left(\frac{\partial w_2}{\partial x}\right)^2+\left(\frac{\partial w_2}{\partial z}\right)^2\right)+\tau\frac{M_0}{\overline{H}}\left(w_2H_3\right)^2. \tag{2.17}$$

Subject to the boundary conditions on the right half of the xz-plane $\{(-\infty<x<\infty, z\geq 0): x, z\in\mathbb{R}\}$:

$$\begin{aligned}&u_1=U_\infty,\quad u_3=0,\quad W=W_0\frac{\partial u_1}{\partial z},\quad T=T_w\quad at\quad z=0,\\ &u_1\to 0,\quad W\to 0,\quad T\to\infty\quad \text{as}\quad z\to\infty.\end{aligned} \tag{2.18}$$

In Eqs. (2.13)-(2.17), u_1 and u_3 are the velocity components in x and z directions, H_1 and H_3 are the magnetic field components, ρ is the density of the medium, μ is the dynamic viscosity, c_p is the specific heat capacitance, T represents the fluid temperature and κ denotes the effective thermal conductivity of the medium. From Eqs. (2.7) and (2.8) we write

$$\bigtriangledown\times H=\sigma(E+v\times B). \tag{2.19}$$

The component form of magnetic flux density in Eq. (2.8) is given by

$$(j_x, j_y, j_z)=\left(0,\sigma\left(u_3B_x-u_1B_z\right),0\right). \tag{2.20}$$

To derive an initial boundary value problem based on the micropolar continuum description with MMR, we make the following assumptions regarding the flow. Consider a convective micropolar flow in a steady, incompressible, laminar, and two-dimensional settings. The flow direction aligns with the x-axis, while the z-axis is oriented perpendicular to this direction as shown in Figure 1. The magnetic field denoted by $H=(0,0,H_0)$ is applied normal to the flow direction. The flow field velocities are assumed $V=(u(x,z),0,0)$, $w=(0,w(x,z),0)$, and $W=(0,w_2,0)$. It should be noted that H_x denotes the induced magnetic field, which implies that the magnetic field vector is represented as $H=(H_1,0,H_3)$. Interpreting equation (2.10) in component form based on the aforementioned flow assumptions yield

$$M_1=\frac{M_0(H_1-\tau H_3\omega_2)}{H_1}=\tau M_0\omega_2,\quad M_2=0, \tag{2.21}$$

and

$$M_3=\frac{M_0(H_3-\tau H_1\omega_2)}{H_1}. \tag{2.22}$$

Also, the magnetic induction vector $\mathbf{B}$ takes the following form

$$(B_1,B_2,B_3)=\left(\tau M_0\omega_2, 0, \mu_0H_0+M_0\right). \tag{2.23}$$

It follows from the above discussion and Eqs. (2.14)-(2.23) that

$$u_1\frac{\partial u_1}{\partial x}+u_3\frac{\partial u_1}{\partial z}=\left(\frac{\mu+\kappa}{\rho}\right)\frac{\partial^2 u_1}{\partial z^2}+\frac{\kappa}{\rho}\frac{\partial w_2}{\partial z}$$
$$-\frac{\sigma}{\rho}\left(\left(\mu_0H_0+M_0\right)\tau M_0u_3W_2+\left(\mu_0H_0+M_0\right)^2u_1\right), \tag{2.24}$$

$$u_1\frac{\partial w_2}{\partial x}+u_3\frac{\partial w_2}{\partial z}=\frac{\gamma^*}{\rho j}\left(\frac{\partial^2 w_2}{\partial z^2}\right)-\frac{k}{\rho j}\left(2w_2+\frac{\partial u_1}{\partial z}\right)-\frac{\tau M_0H_0}{\rho c}w_2 \tag{2.25}$$

and

$$u_1\frac{\partial T}{\partial x}+u_2\frac{\partial T}{\partial z}=\frac{\kappa}{\rho c_p}\left(\frac{\partial^2 T}{\partial z^2}\right)+\frac{\kappa}{\rho c_p}\left(\frac{\partial u_1}{\partial x}+\frac{\partial u_3}{\partial z}\right)+\frac{\mu}{\rho c_p}\left(\frac{\partial u_1}{\partial z}\right)^2+\frac{4\kappa}{\rho c_p}\left(w_2-\frac{1}{2}\frac{\partial u_1}{\partial z}\right)^2+\frac{\tau M_0 H_0^2}{\overline{H}\rho c_p}w_2^2, \tag{2.26}$$

subjected to the associated boundary conditions. Now, let us assume the following boundary layer transformations

$$\begin{aligned}&\xi=z\sqrt{\frac{U_\infty}{\nu x}},\quad \psi=U_\infty\sqrt{\frac{\nu x}{U_\infty}}f(\xi),u_1=U_\infty f'(\xi),\quad u_3=\frac{1}{2}\sqrt{\frac{U_\infty\nu}{x}}(\xi f'(\xi)-f(\xi)),\\&w_2=U_\infty\sqrt{\frac{U_\infty}{\nu x}}R(\xi),\quad \text{and}\quad \theta(\xi)=\frac{T-T_\infty}{T_w-T_\infty}.\end{aligned} \tag{2.27}$$

It is easy to see that after some calculations the Eqs. (2.24)-(2.26) are transformed into the following nonlinear system of coupled ordinary differential equations.

$$(1+K)f'''+KR'-\frac{A}{2}(\xi f'-f)R+Mf'+\frac{ff''}{2}=0, \tag{2.28}$$

$$\left(1+\frac{K}{2}\right)R''-\beta(2R+f'')-ww^*R+\frac{f'R}{2}+\frac{fR'}{2}=0 \tag{2.29}$$

and

$$\frac{1}{Pr}\theta''+(1+K)E_cf''^2+(4K+R_m)E_cR^2-4KE_cRf''+\frac{f\theta'}{2}=0, \tag{2.30}$$

together with the boundary conditions from Eq. (2.18) to

$$\begin{aligned}&f=0,\quad f'=1,\quad R=0,\quad \theta=1\quad at\quad \xi=0,\\&f'=0,\quad R=0,\quad \theta=0\quad as\quad \xi\to\infty.\end{aligned} \tag{2.31}$$

Here, the parameters K, ξ, β, w, M, A, $w*$, R_m, Pr and Ec are dimensionless and are stated as:

$$\begin{aligned}&K=\frac{k}{\mu},\quad \xi=\frac{H_0^2}{c^2l},\quad \left(1+\frac{k}{2}\right)=\frac{\gamma^*}{\rho j},\quad \beta=\frac{k}{\rho j},M=\frac{\sigma}{\rho}\frac{B_0^2}{c},\quad w=\frac{M_0H_0^2}{\rho\overline{H}},\quad w^*=\frac{\tau}{c},\\&R_m=\frac{\tau M_0H_0^2}{\mu\overline{H}},\quad A=\frac{\sigma}{\rho}(\mu_0H_0+M_0)\tau M_0,Pr=\frac{\mu C_p}{k}\quad \text{and}\quad E_c=\frac{U_\infty^2}{C_p(T_w-T_\infty)}.\end{aligned} \tag{2.32}$$

The parameter of physical interest is the skin friction coefficient, defined as

$$C_f=\frac{\tau_w}{\rho u_w^2}, \tag{2.33}$$

where $u_w=cx$ is the characteristic velocity and τ_w is the wall shear stress given by

$$\tau_w=\left[(\mu+k)\frac{\partial u_1}{\partial z}+kW\right]_{z=0}. \tag{2.34}$$

Substituting Eq. (2.27) into Eq. (2.34), the skin friction coefficient in Eq. (2.33) takes the following form

$$C_f\sqrt{Re_x}=(1+K)f''(0)+KR(0). \tag{2.35}$$

The other parameter of practical interest is the Nusselt number defined as

$$Nu_x=\frac{xq_w}{k(T_w-T_\infty)}, \tag{2.36}$$

where q_w is the heat flux given by

$$q_w = -k\frac{\partial T}{\partial z}. \tag{2.37}$$

By using Eq. (2.27) into Eq. (2.37), the Nusselt number in Eq. (2.36) becomes

$$\left(\sqrt{Re_x}\right)^{-1/2} Nu_x = -\theta', \tag{2.38}$$

where $Re_x = \dfrac{u_w x}{\nu}$ is the local Reynolds number.

3. Numerical Method of Solution

To solve the system in Eqs. (2.28)-(2.31), we adopt the finite element numerical procedure. The method is based on the following main steps. First the domain is discretised into finite number of elements. On each element the discretised version of the PDE problem is solved with integration using Gaussian quadrature rule. The solution at each elemental level is achieved with the desired accuracy. The solution for the next element is calculated so that the total number of finite elements is reached. The obtained solution on each element of the mesh is used and assemble of the finite element solution on the complete mesh. To this end, the system of simultaneous nonlinear differential Eqs. (2.28)-(2.31), is first restated by substitution

$$f' = h, \tag{3.1}$$

as

$$(1+K)h'' + KR' - \frac{A}{2}(\xi h - f)R + Mh + \frac{fh'}{2} = 0, \tag{3.2}$$

$$\left(1+\frac{K}{2}\right)R'' - \beta(2R+h') - ww^{*}R + \frac{hR}{2} + \frac{fR'}{2} = 0, \tag{3.3}$$

$$\frac{1}{Pr}\theta'' + (1+K)E_c h'^2 + (4K+R_m)E_c R^2 - 4KE_c Rfh' + \frac{f\theta'}{2} = 0. \tag{3.4}$$

The corresponding boundary conditions thus expressed as

$$\begin{aligned} &f=0,\ h=1,\ R=0,\ \theta=1 \quad at \quad \xi=0,\\ &h=0,\ R=0,\ \theta=0 \quad as \quad \xi\to\infty. \end{aligned} \tag{3.5}$$

To apply the finite element procedure stated above, the system in Eqs. (3.1)-(3.4) first reduced to the weak integral form.

3.1. Weak integral representation and theoretical analysis.

Let us assume that ξ, ϱ, φ, and ϑ, are functions in the polynomial space $\mathbb{P}_2$, as test functions corresponding to the velocity, velocity gradient, microrotation, and temperature field variables, respectively. The variational form associated with Eqs. (3.1)-(3.4) over a typically quadratic element $(\xi_a,\ \xi_{a+1})$ reads:

$$\int_{\xi_a}^{\xi_{a+1}} (f'-h)\cdot\zeta\, d\xi = 0, \quad \forall \quad \xi \in \mathbb{P}_2, \tag{3.6}$$

$$\int_{\xi_a}^{\xi_{a+1}} \left((1+K)h'' + KR' - \frac{A}{2}(\xi h - f)R + Mh + \frac{fh'}{2}\right)\cdot\varphi\, d\xi = 0, \quad \forall \quad \varphi \in \mathbb{P}_2, \tag{3.7}$$

$$\int_{\xi_a}^{\xi_{a+1}} \left(\left(1+\frac{K}{2}\right)R'' - \beta(2R+h') - ww^{*}R + \frac{hR}{2} + \frac{fR'}{2}\right)\cdot\varrho\, d\xi = 0, \quad \forall \quad \varrho \in \mathbb{P}_2 \tag{3.8}$$

and

$$\int_{\xi_a}^{\xi_{a+1}} \left(\frac{1}{Pr}\theta'' + (1+K)E_c h'^2 + (4K+R_m)E_c R^2 - 4KE_c R f h' + \frac{f\theta'}{2} \right) \cdot \vartheta \, d\xi = 0, \quad \forall \quad \vartheta \in \mathbb{P}_2. \tag{3.9}$$

After the application of the Gauss divergence theorem, Eqs. (4.6)-(3.9) becomes

$$\int_{\xi_a}^{\xi_{a+1}} f'\zeta \, d\xi - \int_{\xi_a}^{\xi_{a+1}} h \cdot \zeta \, d\xi = 0, \tag{3.10}$$

$$\int_{\xi_a}^{\xi_{a+1}} \left(KR' - \frac{A}{2}(\xi h - f)R + Mh + \frac{fh'}{2} \right) \cdot \varphi \, d\xi - \int_{\xi_a}^{\xi_{a+1}} (1+K)h'\varphi' \, d\xi = 0, \tag{3.11}$$

$$\int_{\xi_a}^{\xi_{a+1}} \left(-\beta(2R+h') - ww^*R + \frac{hR}{2} + \frac{fR'}{2} \right) \cdot \varrho \, d\xi - \int_{\xi_a}^{\xi_{a+1}} \left(1 + \frac{K}{2}\right) R'\varrho' \, d\xi = 0, \tag{3.12}$$

$$\int_{\xi_a}^{\xi_{a+1}} \left((1+K)E_c h'^2 + (4K+R_m)E_c R^2 - 4KE_c R f h' + \frac{f\theta'}{2} \right) \cdot \vartheta \, d\xi - \int_{\xi_a}^{\xi_{a+1}} \frac{1}{Pr}\theta'\vartheta' \, d\xi = 0. \tag{3.13}$$

Let us denote the elemental domain $\Omega := (\xi_a, \xi_{a+1})$ and $\zeta = \phi_f$, $\phi = \phi_h$, $\varphi = \phi_R$ and $\vartheta = \phi_\theta$. The weak integral system in Eqs. (3.10)-(3.13) is restated as a problem to find $\boldsymbol{u} \in \mathcal{V}$ such that

$$a(\boldsymbol{u}, \boldsymbol{v}) = \ell(\boldsymbol{v}), \quad \forall \boldsymbol{v} \in \mathcal{V}, \tag{3.14}$$

where the bilinear operator $a(\boldsymbol{u}, \boldsymbol{v})$ is given by

$$\begin{aligned} a(\boldsymbol{u}, \boldsymbol{v}) = \int_\Omega \Bigg(& (f'-h)\phi_f + KR'\phi_h - \frac{A}{2}\bar{R}(f - \xi h)\phi_h + Mh\phi_h + \frac{1}{2}\bar{f}h'\phi_h - (1+K)h'\phi_h' \\ & - \beta(2R+h')\phi_R \omega\omega^* R\phi_R + \frac{1}{2}\bar{h}R\phi_R + \frac{1}{2}\bar{f}R'\phi_R - \left(1+\frac{K}{2}\right) R'\phi_R' + (1+K)E_c\bar{h}'h'\phi_\theta \\ & + (4K+R_m)E_c\bar{R}R\phi_\theta - 4KE_c\bar{R}\bar{f}h'\phi_\theta + \frac{1}{2}\bar{f}\theta'\phi_\theta - \frac{1}{Pr}\theta'\phi_\theta' \Bigg) d\xi \end{aligned} \tag{3.15}$$

and the linear operator $\ell(\boldsymbol{v})$ is zero functional in this case. The following result shows the existence of the unique solution to the problem in Eq. (3.14).

Theorem 3.1. *Let $a(\mathbf{u}, \mathbf{v})$ be a bilinear operator defined as in Eq. (3.15) which is continuous and coercive on $\mathcal{V}$ and $\ell(\boldsymbol{v})$ be the bounded linear functional in $\mathcal{V}'$ then there exists a unique $\boldsymbol{u} \in \mathcal{V}$ solving problem in Eq. (3.14) for all $\boldsymbol{v} \in \mathcal{V}$.*

Proof. Let us denote for convenience $f = u_f$, $h = u_h$, $R = u_R$, $\theta = u_\theta$, $\zeta = v_f$, $\phi = v_h$, $\varphi = v)R$ and $\vartheta = v_\theta$ then Eq. (3.15) can be expressed as

$$a(\boldsymbol{u}, \boldsymbol{v}) = a_{prin}(\boldsymbol{u}, \boldsymbol{v}) + a_{low}(\boldsymbol{u}, \boldsymbol{v}) \tag{3.16}$$

where

$$a_{prin}(\boldsymbol{u}, \boldsymbol{v}) = \int_\Omega (a_1 u_h' v_h' + a_2 u_R' v_R' + a_3 u_\theta' v_\theta') \; d\xi \tag{3.17}$$

and

$$\begin{aligned} a_{low}(\boldsymbol{u}, \boldsymbol{v}) = \int_\Omega \Bigg(& (u_h - u_f')v_f - Ku_R'v_R + \frac{A}{2}\bar{u_R}(\xi u_h - u_f)v_h - Mu_h v_h - \frac{1}{2}\bar{u_f}u_h'v_h \\ & + \beta(2u_R + u_h')v_R + \omega\omega^* u_R v_R - \frac{1}{2}\bar{u_h}u_R v_R - \frac{1}{2}\bar{u_f}u_R'v_R - (1+K)E_c\bar{u_h'}u_h'v_\theta \\ & - (4K+R_m)E_c\bar{u_R}u_R v_\theta + 4KE_c\bar{u_R}\bar{u_f}u_h'v_\theta - \frac{1}{2}\bar{u_f}u_\theta'v_\theta \Bigg) d\xi, \end{aligned} \tag{3.18}$$

with $a_1 = (1+K)$, $a_2 = \left(1+\frac{K}{2}\right)$ and $a_3 = \frac{1}{Pr}$. Suppose

$$\exists \quad C_{min} > 0 \quad \text{s.t. almost everywhere on} \quad \Omega \quad a_i \geq C_{min} \quad \text{for} \quad \text{i} = 1,\, 2,\, 3.$$

Then

$$\begin{aligned} a_{prin}(\boldsymbol{u}, \boldsymbol{u}) &= \int_\Omega \left(a_1|u_h'|^2 + a_2|u_R'|^2 + a_3|u_\theta'|^2\right)\, d\xi \\ &\geq C_{min} \sum_{j=1} \|w_j'\|^2_{L^2(\Omega)} = C_{min}|w|_1^2; \quad j \in \{h, R, \theta\} \end{aligned} \tag{3.19}$$

where we define the energy seminorm

$$|w|_1^2 := \sum_{j\in\{h,R,\theta\}} \|w_j'\|^2_{L^2(\Omega)} \tag{3.20}$$

This gives a lower bound for the a_{prin} in terms of the H^1-seminorm. We now bound a_{low} in terms of $|w|_1^2$. The terms in a_{low} are finite sums of integrals of the form

$$I_b^{pq} := \int_\Omega b_{pq}(\xi) w_p'(\xi) w_q(\xi)\, d\xi; \quad p, q \in \{f, h, R, \theta\}$$

and

$$I_d^{pq} := \int_\Omega d_{pq}(\xi) w_p(\xi) w_q(\xi)\, d\xi$$

with $b_{pq}, d_{pq} \in L^\infty(\Omega)$. Also

$$\begin{aligned} |I_d^{pq}| = \Bigg| \int_\Omega \Bigg(& u_h v_f - \frac{A}{2}\bar{u_R}(\xi u_h - u_f)v_h - M u_h v_h + \beta 2 u_R v_R \\ & + \omega\omega^* u_R v_R - \frac{1}{2}\bar{u_h} u_R v_R - (4K + R_m) E_c \bar{u_R} u_R v_\theta \Bigg) d\xi \Bigg| \\ \leq\; & \|d_{pq}\|_\infty \|w_p\|_{L^2(\Omega)} \|w_q\|_{L^2(\Omega)} \quad \text{(Cauchy Schwarz Inequality)} \\ \leq\; & \|d_{pq}\|_\infty C_p^2 \|w_p'\|_{L^2(\Omega)} \|w_q'\|_{L^2(\Omega)} \quad \text{for some} \quad C_p \in \mathbb{R} \quad \text{(Poincaré Inequality)} \\ \leq\; & \|d_{pq}\|_\infty C_p^2 \left(\epsilon \|w_p'\|^2_{L^2(\Omega)} + \frac{1}{4\epsilon}\|w_q'\|^2_{L^2(\Omega)}\right) \quad \text{for some} \quad \epsilon > 0 \quad \text{(Young's Inequality)}, \end{aligned} \tag{3.21}$$

$$\implies |I_d^{pq}| \leq C_p^2 \|d_{pq}\|_\infty \left(\epsilon \|w_p'\|^2_{L^2(\Omega)} + \frac{1}{4\epsilon}\|w_q'\|^2_{L^2(\Omega)}\right) \tag{3.22}$$

Similarly

$$\begin{aligned} |I_b^{pq}| &\leq \|b_{pq}\|_\infty \|w_p'\|_{L^2(\Omega)} \|w_q\|_{L^2(\Omega)} \\ &\leq \|b_{pq}\|_\infty C_p \|w_p'\|_{L^2(\Omega)} \|w_q'\|_{L^2(\Omega)} \\ &\leq \|b_{pq}\|_\infty C_p \left(\epsilon_1 \|w_p'\|^2_{L^2(\Omega)} + \frac{1}{4\epsilon_1}\|w_q'\|^2_{L^2(\Omega)}\right) \quad \text{for some} \quad \epsilon_1 > 0. \end{aligned} \tag{3.23}$$

By summing all such bounds over all index pairs (i, j) with

$$B := \max_{pq} \|b_{pq}\|_\infty, \quad D := \max_{pq} \|d_{pq}\|_\infty$$

and collecting the estimates in Eq. (3.22) and Eq. (3.24) we write

$$a(\boldsymbol{u}, \boldsymbol{u}) \geq C_{min}|u|_1^2 - \beta |u|_1^2 = (C_{min} - \beta)|u|_1^2. \tag{3.24}$$

Since C_{min} is the minimal positive number of the diffusion-like coefficients $\left(1+K, 1+\frac{K}{2},\right.$ and $\left.\frac{1}{Pr}\right)$ which are positive numbers and β measure the aggregate strength of the lower-order coupling coefficients scaled by C_p, therefore C_p can be chosen such that $(C_{min} - \beta) > 0$. Thus a is coercive on $\mathcal{V}$. Next we need to show that a is continuous on $\mathcal{V}$ equipped with H^1-norm. Since each term in $a(w,v)$ is an integral of products of bounded coefficients and either derivatives or functions, by using Cauchy-Schwarz and Poincaré inequalities as before we can thus write

$$\left|\int_\Omega a_p w_p' v_p'\right| \leq \|a_p\|_\infty \|w_p'\|_{L^2(\Omega)} \|v_p'\|_{L^2(\Omega)} \leq \|a_p\|_\infty \|w\|_{H^1(\Omega)} \|v\|_{H^1(\Omega)}, \tag{3.25}$$

$$\left|\int_\Omega b_{pq} w_p' v_q\right| \leq \|b_{pq}\|_\infty \|w_p'\|_{L^2(\Omega)} \|v_q\|_{L^2(\Omega)} \leq \|b_{pq}\|_\infty C_p \|w\|_{H^1(\Omega)} \|v\|_{H^1(\Omega)} \tag{3.26}$$

and

$$\left|\int_\Omega d_{pq} w_p v_q\right| \leq \|d_{pq}\|_\infty \|w_p\|_{L^2(\Omega)} \|v_q\|_{L^2(\Omega)} \leq \|d_{pq}\|_\infty C_p^2 \|w\|_{H^1(\Omega)} \|v\|_{H^1(\Omega)}. \tag{3.27}$$

Summing Eqs. (3.25)-(3.27) over all pairs (p,q) we can find a finite constant C_{cont} such that

$$|a(w,v)| \leq C_{\text{cont}} \|w\|_{H^1(\Omega)} \|v\|_{H^1(\Omega)}.$$

Thus a is continuous on $\mathcal{V}$ equipped with H^1-norm. This completes the proof. □

3.2. **Discrete finite element formulation.** The discrete form of the problem corresponding to the system in Eqs. (3.10)-(3.13) is obtained by the substitution of the following nodal contributions

$$f = \sum_{j=1}^{n} f_j \psi_j, \quad h = \sum_{j=1}^{n} h_j \psi_j, \quad R = \sum_{j=1}^{n} R_j \psi_j \quad \text{and} \quad \theta = \sum_{j=1}^{n} \theta_j \psi_j, \tag{3.28}$$

where n is the total number of nodes in an element. Further, assume that $\zeta = \varphi = \varrho = \vartheta = \psi_i$, (for $i = 1,2,3$), where ψ_i are the shape functions for a two-noded quadratic element (ξ_a, ξ_{a+1}) expressed by

$$\psi_1^{(a)} = \frac{(\xi_{a+1} + \xi_a - 2\xi)(\xi_{a+1} - \xi)}{(\xi_{a+1} - \xi_a)^2}, \quad \psi_2^{(a)} = \frac{4(\xi - \xi_a)(\xi_{a+1} - \xi)}{(\xi_{a+1} - \xi_a)^2}$$
$$\text{and} \quad \psi_3^{(a)} = \frac{(\xi_{a+1} + \xi_a - 2\xi)(\xi - \xi_a)}{(\xi_{a+1} - \xi_a)^2}, \quad \text{for} \quad \xi_a \leq \xi \leq \xi_{a+1}. \tag{3.29}$$

Using Eq. (3.28) and (3.29) in Eqs. (3.10)-(3.13) the following system of matrix vector equation is obtained for each element e.

$$\begin{bmatrix}
K_{11}^{11} & K_{12}^{11} & K_{13}^{11} & K_{11}^{12} & K_{12}^{12} & K_{13}^{12} & K_{11}^{13} & K_{12}^{13} & K_{13}^{13} & K_{11}^{14} & K_{12}^{14} & K_{13}^{14} \\
K_{21}^{11} & K_{22}^{11} & K_{23}^{11} & K_{21}^{12} & K_{22}^{12} & K_{23}^{12} & K_{21}^{13} & K_{22}^{13} & K_{23}^{13} & K_{21}^{14} & K_{22}^{14} & K_{23}^{14} \\
K_{31}^{11} & K_{32}^{11} & K_{33}^{11} & K_{31}^{12} & K_{32}^{12} & K_{33}^{12} & K_{31}^{13} & K_{32}^{13} & K_{33}^{13} & K_{31}^{14} & K_{32}^{14} & K_{33}^{14} \\
K_{11}^{21} & K_{12}^{21} & K_{13}^{21} & K_{11}^{22} & K_{12}^{22} & K_{13}^{22} & K_{11}^{23} & K_{12}^{23} & K_{13}^{23} & K_{11}^{24} & K_{12}^{24} & K_{13}^{24} \\
K_{21}^{21} & K_{22}^{21} & K_{23}^{21} & K_{21}^{22} & K_{22}^{22} & K_{23}^{22} & K_{21}^{23} & K_{22}^{23} & K_{23}^{23} & K_{21}^{24} & K_{22}^{24} & K_{23}^{24} \\
K_{31}^{21} & K_{32}^{21} & K_{33}^{21} & K_{31}^{22} & K_{32}^{22} & K_{33}^{22} & K_{31}^{23} & K_{32}^{23} & K_{33}^{23} & K_{31}^{24} & K_{32}^{24} & K_{33}^{24} \\
K_{11}^{31} & K_{12}^{31} & K_{13}^{31} & K_{11}^{32} & K_{12}^{32} & K_{13}^{32} & K_{11}^{33} & K_{12}^{33} & K_{13}^{33} & K_{11}^{34} & K_{12}^{34} & K_{13}^{34} \\
K_{21}^{31} & K_{22}^{31} & K_{23}^{31} & K_{21}^{32} & K_{22}^{32} & K_{23}^{32} & K_{21}^{33} & K_{22}^{33} & K_{23}^{33} & K_{21}^{34} & K_{22}^{34} & K_{23}^{34} \\
K_{31}^{31} & K_{32}^{31} & K_{33}^{31} & K_{31}^{32} & K_{32}^{32} & K_{33}^{32} & K_{31}^{33} & K_{32}^{33} & K_{33}^{33} & K_{31}^{34} & K_{32}^{34} & K_{33}^{34} \\
K_{11}^{41} & K_{12}^{41} & K_{13}^{41} & K_{11}^{42} & K_{12}^{42} & K_{13}^{42} & K_{11}^{43} & K_{12}^{43} & K_{13}^{43} & K_{11}^{44} & K_{12}^{44} & K_{13}^{44} \\
K_{21}^{41} & K_{22}^{41} & K_{23}^{41} & K_{21}^{42} & K_{22}^{42} & K_{23}^{42} & K_{21}^{43} & K_{22}^{43} & K_{23}^{43} & K_{21}^{44} & K_{22}^{44} & K_{23}^{44} \\
K_{31}^{41} & K_{32}^{41} & K_{33}^{41} & K_{31}^{42} & K_{32}^{42} & K_{33}^{42} & K_{31}^{43} & K_{32}^{43} & K_{33}^{43} & K_{31}^{44} & K_{32}^{44} & K_{33}^{44}
\end{bmatrix}
\begin{bmatrix} f_1^e \\ f_2^e \\ f_3^e \\ h_1^e \\ h_2^e \\ h_3^e \\ R_1^e \\ R_2^e \\ R_3^e \\ \theta_1^e \\ \theta_2^e \\ \theta_3^e \end{bmatrix}
=
\begin{bmatrix} b_1^1 \\ b_2^1 \\ b_3^1 \\ b_1^2 \\ b_2^2 \\ b_3^2 \\ b_1^3 \\ b_2^3 \\ b_3^3 \\ b_1^4 \\ b_2^4 \\ b_3^4 \end{bmatrix}. \tag{3.30}$$

In Eq. (3.30), the sub-matrices K_{ij}^{mn} (with $m,n \in \{1,2,3,4\}$; $i,j \in \{1,2,3\}$) and the vectors b_i^m are defined as

$$K_{ij}^{11} = \int_{\xi_a}^{\xi_{a+1}} \psi_i \frac{d\psi_j}{d\xi} d\xi, \; K_{ij}^{12} = -\int_{\xi_a}^{\xi_{a+1}} \psi_i \psi_j d\xi, \; K_{ij}^{13} = K_{ij}^{14} = K_{ij}^{24} = K_{ij}^{34} = 0, \tag{3.31}$$

$$K_{ij}^{21} = \frac{A}{2} \int_{\xi_a}^{\xi_{a+1}} \overline{R} \psi_i \psi_j d\xi + \frac{1}{2} \int_{\xi_a}^{\xi_{a+1}} \overline{h'} \psi_i \psi_j d\xi, \tag{3.32}$$

$$K_{ij}^{22} = -(1+K)\int_{\xi_a}^{\xi_{a+1}} \frac{d\psi_i}{d\xi}\frac{d\psi_j}{d\xi}d\xi - \frac{A\xi}{2}\int_{\xi_a}^{\xi_{a+1}} \overline{R}\psi_i\psi_j d\xi + M\int_{\xi_a}^{\xi_{a+1}} \psi_i\psi_j d\xi + \frac{1}{2}\int_{\xi_a}^{\xi_{a+1}} \overline{f}\psi_i\frac{d\psi_j}{d\xi}d\xi, \tag{3.33}$$

$$K_{ij}^{23} = K\int_{\xi_a}^{\xi_{a+1}} \psi_i\frac{d\psi_j}{d\xi}d\xi - \frac{A\xi}{2}\int_{\xi_a}^{\xi_{a+1}} \overline{h}\psi_i\psi_j d\xi + \frac{A}{2}\int_{\xi_a}^{\xi_{a+1}} \overline{f}\psi_i\psi_j d\xi, \tag{3.34}$$

$$K_{ij}^{31} = \frac{1}{2}\int_{\xi_a}^{\xi_{a+1}} \overline{R'}\psi_i\psi_j d\xi, \quad K_{ij}^{32} = -\beta\int_{\xi_a}^{\xi_{a+1}} \psi_i\frac{d\psi_j}{d\xi}d\xi + \frac{1}{2}\int_{\xi_a}^{\xi_{a+1}} \overline{R}\psi_i\psi_j d\xi, \tag{3.35}$$

$$\begin{aligned}K_{ij}^{33} = &-\left(1+\frac{K}{2}\right)\int_{\xi_a}^{\xi_{a+1}} \frac{d\psi_i}{d\xi}\frac{d\psi_j}{d\xi}d\xi - 2\beta\int_{\xi_a}^{\xi_{a+1}} \psi_i\psi_j d\xi - ww^*\int_{\xi_a}^{\xi_{a+1}} \psi_i\psi_j d\xi\\ &+\frac{1}{2}\int_{\xi_a}^{\xi_{a+1}} \overline{h}\psi_i\psi_j d\xi + \frac{1}{2}\int_{\xi_a}^{\xi_{a+1}} \overline{f}\psi_i\frac{d\psi_j}{d\xi}d\xi,\end{aligned} \tag{3.36}$$

$$K_{ij}^{41} = \frac{1}{2}\int_{\xi_a}^{\xi_{a+1}} \overline{\theta'}\psi_i\psi_j d\xi, \; K_{ij}^{42} = 2KE_c\int_{\xi_a}^{\xi_{a+1}} \overline{h'}\psi_i\frac{d\psi_j}{d\xi}d\xi + 4KE_c\int_{\xi_a}^{\xi_{a+1}} \overline{R}\psi_i\frac{d\psi_j}{d\xi}d\xi, \tag{3.37}$$

$$K_{ij}^{43} = 4KE_c\int_{\xi_a}^{\xi_{a+1}} \overline{R}\psi_i\psi_j d\xi + RmE_c\int_{\xi_a}^{\xi_{a+1}} \overline{R}\psi_i\psi_j d\xi + 4KE_c\int_{\xi_a}^{\xi_{a+1}} \overline{h'}\psi_i\psi_j d\xi, \tag{3.38}$$

$$K_{ij}^{44} = -\frac{1}{Pr}\int_{\xi_a}^{\xi_{a+1}} \frac{d\psi_i}{d\xi}\frac{d\psi_j}{d\xi}d\xi + \frac{1}{2}\int_{\xi_a}^{\xi_{a+1}} \overline{f}\psi_i\frac{d\psi_j}{d\xi}d\xi, \tag{3.39}$$

where in Eqs. (3.31)-(3.39)

$$\overline{f} = \sum_{j=1}^{n}\overline{f}_j\psi_j, \quad \overline{h} = \sum_{j=1}^{n}\overline{h}_j\psi_j, \quad \overline{h'} = \sum_{j=1}^{n}\overline{h'}_j\psi_j, \quad \overline{R} = \sum_{j=1}^{n}\overline{R}_j\psi_j, \quad \overline{R'} = \sum_{j=1}^{n}\overline{R'}_j\psi_j, \quad \overline{\theta'} = \sum_{j=1}^{n}\overline{\theta'}_j\psi_j,$$

$$b_i^1 = 0, \;\; b_i^2 = -(1+K)\left(\psi\frac{dh}{d\xi}\right)_{\xi_a}^{\xi_{a+1}}, \;\; b_i^3 = -\left(1+\frac{K}{2}\right)\left(\psi\frac{dR}{d\xi}\right)_{\xi_a}^{\xi_{a+1}} \;\text{ and }\; b_i^4 = -\frac{1}{Pr}\left(\psi\frac{d\theta}{d\xi}\right)_{\xi_a}^{\xi_{a+1}}.$$

To implement the proposed model an open source code FreeFEM++ [12] is utilized. To calculate f, h, R and θ the following numerical algorithm is utilized.

Numerical Algorithm:

Step 1: Define the domain using the `border` command in FreeFEM++.
Step 2: Discretize the domain into quadratic finite elements using the command `buildmesh`. The mesh is generated using the Delaunay-Voronoi algorithm.
Step 3: Define the finite element space using the command `fespace` with f, h, R, and θ as continuous piecewise quadratic functions in $\mathbb{P}_2$.
Step 4: Solve the system.
  Step 4.1. Set the length $d\xi$ of the finite element e.
  Step 4.2. Choose the element number as $e = 1$.
  Step 4.3. Initialize the physical parameters K, Pr, ω, A, ξ, Ec, ω^*, Rm, M and β.
  Step 4.4. Loop over the number of finite elements $'ne'$.
  Step 4.5. Initialize f, h, R and θ with zero.
  Step 4.6. Construct the stiffness matrix $\boldsymbol{K}$ and load vector $\boldsymbol{Q}$ as in Eq. (3.30) with the help of the `varf` command.
  Step 4.7. Update the element number $e = e + 1$ and go to Step 4.5.

Step 4.8. Solve the global system obtained in Step 4.5 by calling the UMFPACK library.
Step 4.9. Check the convergence criterion of the solution. If reached, save the solution for post-processing; otherwise, update the solution and go to Step 4.5.
Step 5: Save the solution data for post-processing.

4. RESULTS AND DISCUSSIONS

In this section, the results obtained by computing the MMR-IBVP model in Eqs. (3.1)-(3.5) are presented. Numerical experiments are performed for different values of the material parameters to calculate the translational, rotational velocity, and temperature field profiles. Moreover, the physical parameters of interest the skin-friction coefficient and the Nusselt number are also calculated. In the present study, the computational domain is restricted to a finite region based on the physical characteristics of the boundary-layer flow. Since the velocity, microrotation, and thermal fields asymptotically approach their free-stream values beyond a certain distance, enlarging the domain further does not meaningfully influence the solution within the boundary layer. This was verified by conducting domain-sensitivity tests, where the domain length was increased until the computed profiles stabilized. The selected domain length i.e. $\xi_\infty = 12$, thus ensures computational efficiency without compromising solution accuracy. To verify the accuracy and stability of the numerical scheme, a detailed convergence study is carried out using non-uniform mesh refinements. Order of convergence (p_m) is computed using the successive differences of the skin-friction coefficient (Sf). Let us define

TABLE 1. Skin-friction values with varying number of triangles and vertices.

Mesh Level (m)	Number of Elements	Number of Vertices	Skin-friction coefficient (Sf)	$\lvert Sf_{m+1} - Sf_m\rvert$
1	40	33	-0.72353710	–
2	100	64	-0.68986571	0.03367139
3	400	217	-0.68389345	0.00387621
4	900	405	-0.68143392	0.00245953
5	1360	793	-0.68067575	0.00075817
6	3780	1548	-0.68020963	0.00046612
7	5580	3025	-0.67998188	0.00022775
8	10062	5313	-0.67988624	9.56366×10^{-5}

$$\Delta_m = \left|Sf_{m+1} - Sf_m\right|, \qquad \Delta_{m+1} = \left|Sf_{m+2} - Sf_{m+1}\right|, \tag{4.1}$$

where Δ_m and Δ_{m+1} represent the absolute differences in the computed values of Sf between three successive mesh levels m, $m+1$, and $m+2$. If h_m denotes the characteristic mesh size and $r_m = \dfrac{h_m}{h_{m+1}}$ is the refinement ratio, the order of convergence is computed as

$$p_m = \ln\left(\frac{\Delta_m}{\Delta_{m+1}}\right) \Bigg/ \ln(r_m). \tag{4.2}$$

In this case the total number of triangular elements N are known, we assume $h \sim N^{-1/2}$, giving

$$r_m \approx \sqrt{\frac{N_{m+1}}{N_m}} \quad \Longrightarrow \quad p_m = 2\,\ln\left(\frac{\Delta_m}{\Delta_{m+1}}\right) \Bigg/ \ln\left(\frac{N_{m+1}}{N_m}\right). \tag{4.3}$$

Table 1 illustrates the convergence of the skin-friction coefficient (Sf) and its successive differences $|Sf_{m+1} - Sf_m|$, which decrease as the mesh is refined. The computed values of p_m are summarized in Table 2. It is observed that although the local convergence orders fluctuate due to non-uniform refinement ratios, the overall trend consistently shows a significant reduction in the differences Δ_m, decreasing from 3.37×10^{-2} on the coarsest mesh to 9.56×10^{-5} on the finest mesh. This reduction by more than two orders of magnitude clearly confirms that the computed solutions converge as the mesh is refined. Furthermore, a global least-squares fit of $\log(\Delta_m)$ versus $\log(N_m)$ over all mesh levels shows an effective overall convergence rate of approximately $p \approx 2.4$, which demonstrates that the adopted

Table 2. Order of convergence computed using successive mesh refinements.

Interval	N_m	N_{m+1}	Δ_m	Δ_{m+1}	**Observed order** p_m
1–2–3	40	100	3.367139×10^{-2}	3.87621×10^{-3}	4.719
2–3–4	100	400	3.87621×10^{-3}	2.45953×10^{-3}	0.656
3–4–5	400	900	2.45953×10^{-3}	7.5817×10^{-4}	2.902
4–5–6	900	1360	7.5817×10^{-4}	4.6612×10^{-4}	2.357
5–6–7	1360	3780	4.6612×10^{-4}	2.2775×10^{-4}	1.401
6–7–8	3780	5580	2.2775×10^{-4}	9.56366×10^{-5}	4.456

Table 3. Mesh independence of the computed solutions.

Mesh Level	Number of Elements	$f'(1.0)$	$R(1.0)$	$\theta(1.0)$
1	100	0.426969	0.352044	0.718472
2	400	0.433254	0.360726	0.723433
3	900	0.433755	0.35773	0.725314
4	1360	0.434252	0.357119	0.725743
5	2100	0.434704	0.357109	0.725861
6	3780	0.435098	0.356878	0.726015
7	5580	0.435256	0.356867	0.726058
8	10062	0.435257	0.356855	0.726078

finite element formulation achieves a rate of convergence close to second-order accuracy. Based on these results, mesh levels beyond $m = 6$ provide sufficiently accurate and mesh-independent solutions, ensuring numerical reliability of the reported results in this investigation. To obtain a mesh independent solution several other tests have also been carried out. The grid used to compute the solution is refined with eight different mesh levels. It is observed from Table 3, that the solution in case of velocity, microrotation and temperature fields do not vary significantly after the seventh mesh refinement level. Therefore, in this discussion the mesh taken to compute the solutions is having 10062 number of finite elements. In order to validate the accuracy of computations performed by the presented method for the proposed model problem we compare our results in a limiting case. If we set $K = 0$, $A = M = 0$, $R \equiv 0$, $\theta \equiv 0$ and $E_c = 0$, the system in Eqs. (2.28)-(2.31) reduces to the following classical Blasius boundary-layer problem.

$$f'''(\xi) + \frac{1}{2} f(\xi) f''(\xi) = 0, \tag{4.4}$$

along with the boundary conditions

$$f(0) = 0, \quad f'(0) = 0 \text{ and } f'(\infty) = 1. \tag{4.5}$$

Here, ξ is as in Eq. (2.27). To develop the weak form of the problem in Eqs. (4.4)-(4.5), Let $\phi(\xi)$ be a test function such that $\phi \in H^1(\Omega)$ with $\phi(0) = 0$ and $\phi(\xi_\infty) = 0$. The value ξ_∞ is chosen such that the boundary layer is assumed completely developed. Multiplying Eq. (4.4) by ϕ and integrating over the domain $\Omega = (0, \xi_\infty)$, we obtain

$$\int_0^{\xi_\infty} \left(f'''(\xi) + \frac{1}{2} f(\xi) f''(\xi) \right) \phi(\xi)\, d\xi = 0. \tag{4.6}$$

For the first term, applying integration by parts repeatedly gives

$$\int_0^{\xi_\infty} f'''(\xi)\,\phi(\xi)\,d\xi = \Big[f''(\xi)\phi(\xi)\Big]_0^{\xi_\infty} - \int_0^{\xi_\infty} f''(\xi)\phi'(\xi)\,d\xi \tag{4.7}$$

$$= -\int_0^{\xi_\infty} f''(\xi)\phi'(\xi)\,d\xi, \tag{4.8}$$

since the boundary terms vanish due to $\phi(0) = \phi(\xi_\infty) = 0$. The weak formulation thus reads:
Find $f \in \mathcal{V}$ such that

$$-\int_0^{\xi_\infty} f''(\xi)\,\phi'(\xi)\,d\xi + \frac{1}{2}\int_0^{\xi_\infty} f(\xi)f''(\xi)\phi(\xi)\,d\xi = 0, \quad \forall \phi \in \mathcal{V}, \tag{4.9}$$

where $\mathcal{V} = \{v \in H^1(0,\xi_\infty) \mid v(0) = v(\xi_\infty) = 0\}$ is the space of admissible test functions. To verify and validate the accuracy of the implemented method the above presented classical Blasius boundary-layer problem is computed using the presented method and the method by Kierzenka and Shampine [16]. It can be seen from Table 4 that a strong agreement is achieved between the computed solution for velocity and wall-stress functions with the presented method and the other solutions [16, 20] in the literature. In Table 5, the skin-friction coefficient values are presented against the varying set of material parameters. It delineate the impact of micropolar constant K, MMR parameter A, the viscosity ration factor β and the time relaxation factor ω^* on the skin-friction coefficient. It can be seen that for an increasing values of micropolar constant and viscosity parameter, the skin-friction is directly proportional to β and inversely proportional to K. Moreover, it is observed that for increasing values of the MMR parameter, the skin friction increases. In Table 6, the impact of different physical parameters are taken to observe the effect on Nusselt number. The material parameters varied are the micropolar constant K, magnetic Reynolds number Rm, Eckert number Ec, viscosity ratio parameter β, Prandtl number Pr, and the magnetization relaxation factor ω^*. It is seen that with an increase in the micropolar constant the Nusselt number decreases. This is because increasing the micropolar constant decreases the Nusselt number and reduces convective heat transfer by increasing fluid resistance to shear and heat transfer due to microstructural factors. This tendency is often seen in analysis of micropolar or non-Newtonian fluids with complex thermal and dynamical interactions. Increase in the magnetic Reynolds number leads to an increased value of the Nusselt number. A high magnetic Reynolds number implies stronger coupling between the fluid motion and the magnetic field. Increasing the magnetic Reynolds' number generally suppresses convective heat transfer thereby reducing the Nusselt number. It is also observed from Table 6, that higher Eckert number leads to an increase in the Nusselt number. This is due to the fact that at higher Eckert number the viscous dissipation is enhanced and greater temperature gradients arises at the wall. Also it can be seen that with an increase in the viscosity ratio parameter the Nusselt number is increased. Moreover, the Nusselt number increases with an increase in the Prandtl number. This is because an increase in the Prandtl number enhances the convective heat transfer capability, leading

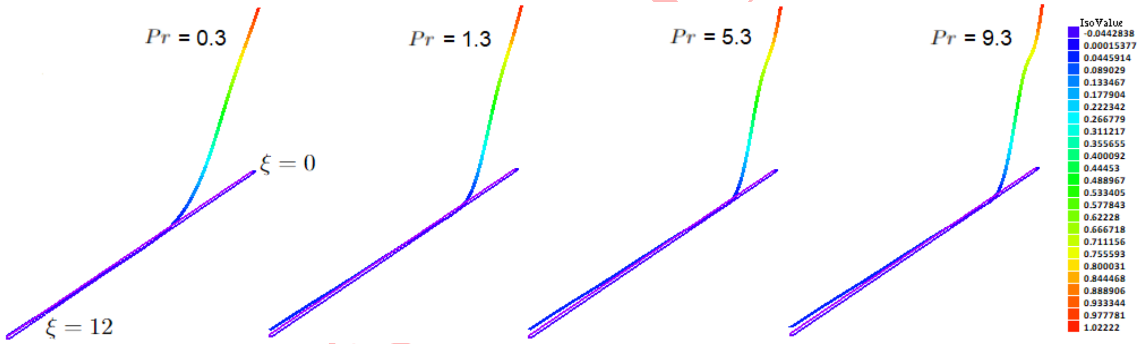

FIGURE 2. Temperature for varying values of the Prandtl number. Other parameters used are: $A = -0.5$, $K = 0.5$, $\beta = 0.5$, $M = 0.1$, ω = -0.5, $\omega^* = 5.5$, $Ec = 0.1$ and $R_m = 9$.

Table 4. Comparison of the numerical results with other solutions in the limiting case.

	Blasius Solution [20]	Present Method	Kierzenka and Shampine [16]	Present Method
ξ	$f'(\xi)$	$f'(\xi)$	$f''(\xi)$	$f''(\xi)$
0.00	0.00000	0.00000012	0.33200	0.33200048
0.20	0.06641	0.06641037	0.33193	0.33193092
0.40	0.13277	0.13277056	0.33142	0.33141987
0.60	0.19984	0.19984073	0.33003	0.33003055
0.80	0.26472	0.26472044	0.32735	0.32734986
1.00	0.32980	0.32980091	0.32298	0.32297964
1.20	0.39381	0.39381038	0.31657	0.31657022
1.40	0.45631	0.45631074	0.30785	0.30784995
1.60	0.51683	0.51683029	0.29666	0.29665987
1.80	0.57486	0.57486065	0.28294	0.28294073
2.00	0.62989	0.62989048	0.26676	0.26675998
2.20	0.68147	0.68147036	0.24836	0.24835984
2.40	0.72918	0.72918052	0.22810	0.22810037
2.60	0.77269	0.77269081	0.20646	0.20645992
2.80	0.81178	0.81178034	0.18400	0.18400046
3.00	0.84634	0.84634057	0.16134	0.16134083
3.20	0.87641	0.87641009	0.13909	0.13909019
3.40	0.90211	0.90211045	0.11782	0.11781995
3.60	0.92370	0.92370028	0.09802	0.09802031
3.80	0.94151	0.94151076	0.08004	0.08003988
4.00	0.95592	0.95592034	0.06414	0.06413974
4.20	0.96736	0.96736089	0.05042	0.05042017
4.40	0.97628	0.97628013	0.03887	0.03887042
4.60	0.98309	0.98309066	0.02938	0.02937981
4.80	0.98819	0.98819023	0.02177	0.02177005
5.00	0.99184	0.99184047	0.01580	0.01579986
5.20	0.99459	0.99459065	0.01124	0.01123978
5.40	0.99655	0.99655019	0.00784	0.00784034
5.60	0.99787	0.99787054	0.00535	0.00534992
5.80	0.99876	0.99876031	0.00357	0.00356988
6.00	0.99936	0.99936008	0.00233	0.00232995

to an increase in the Nusselt number. Further, it is seen that with an increase in the magnetization relaxation factor the Nusselt number is decreased. In Figure 2, the effects of Prandtl number on the temperature distribution are shown. Results indicate that the fluid temperature decreases as Prandtl number increases in magnitude. It leads to a decline in the fluid's thermal conductivity. The temperature field decreases as the Prandtl increases as a result of the fluid's thermal conductance being reduced. The behavior of temperature, rotational and translational velocity profiles in the micropolar fluids is strongly influenced by the micropolar parameter. These fluids are characterized by the existence of microstructure effects and both translational and rotational motions of the fluid particles. They can simulate complex materials such as liquid crystals, polymer solutions, and some biological fluids. With an increase in micropolar constant K, the translational velocity tends to decrease. This is so that translational motion is resisted by increased couple stresses, which increase internal friction in the fluid. Higher couple stresses cause the fluid to become more resistant to flow, which slows down translational velocity. In Figure 3, the influence of micropolar constant is seen on the development of velocity boundary layer profiles. The thickness of the fluid's velocity layer increases as the magnitude of micropolar constant K increases. The behavior of thermal boundary profiles are depicted in Figure 4,

Table 5. Skin-friction coefficient $C_f\sqrt{Re_x}$ for varying physical parameters.

K	A	β	ω^*	Skin-friction
0	1.0	1.0	0.5	-0.393429
1.3				-0.844549
1.7				-0.873079
2.0				-0.898842
	0			-0.882465
	-1.0			-0.912955
	-2.0			-0.93555
	-3.0			-0.952135
		1		-0.952135
		3		-0.896252
		5		-0.847591
		7		-0.813297
			1	-0.866587
			5	-0.944505
			10	-0.942058
			15	-0.935583

Table 6. Nusselt number Nu for varying physical parameters.

K	R_m	Ec	β	Pr	ω^*	Nusselt number
1.3	0.5	0.1	1.0	0.3	0.5	0.327834
1.7						0.305859
2.0						0.296394
2.5						0.286149
2	1					0.296636
	1.5					0.296878
	2.0					0.29712
	2.5					0.297362
		0.3				0.323021
		0.5				0.348679
		0.7				0.374337
		0.9				0.399996
			1.5			0.440681
			2.0			0.478766
			2.5			0.513903
			3.0			0.546152
				1.3		1.48742
				2.3		2.19377
				3.3		2.80085
				4.3		3.34692
					1.5	2.40209
					2.5	2.09635
					3.5	1.94792
					4.5	1.86072

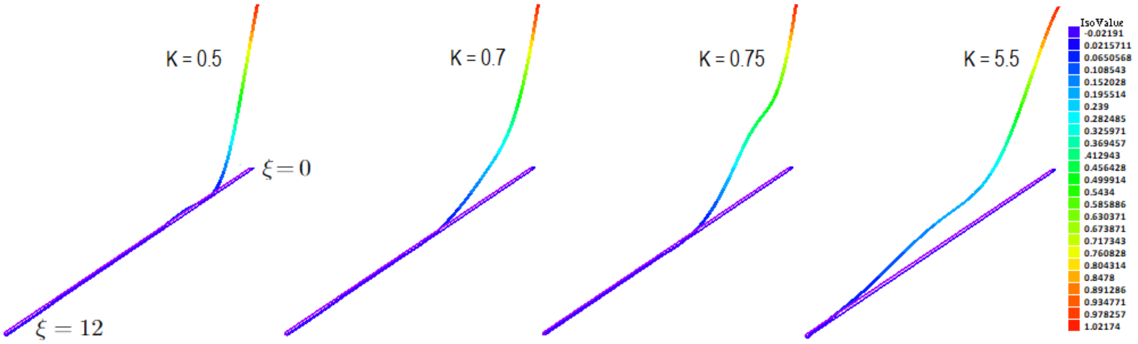

FIGURE 3. Translational velocity for varying values of the micropolar parameter. Other values of physical parameters are assumed as: $K = 0.7$, $\beta = 0.5$, $M = 0.1$, $\omega = -0.5$, $\omega^* = 5.5$, $Pr = 0.3$, $Ec = 0.1$ and $R_m = 1.0$.

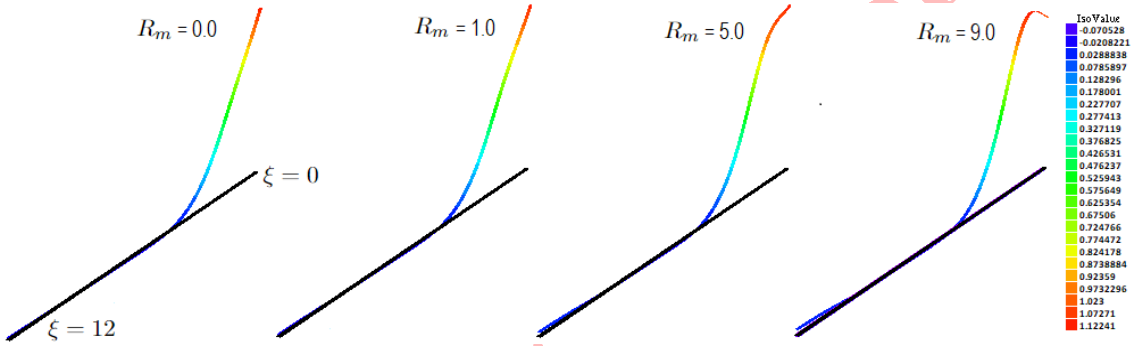

FIGURE 4. Temperature for varying values of the relaxation magnetization factor. Other values of physical parameters are taken as: $A = -0.5$, $K = 0.7$, $\beta = 0.5$, $M = 0.1$, $\omega = -0.5$, $\omega^* = 5.5$, $Pr = 0.3$ and $E_c = 0.1$.

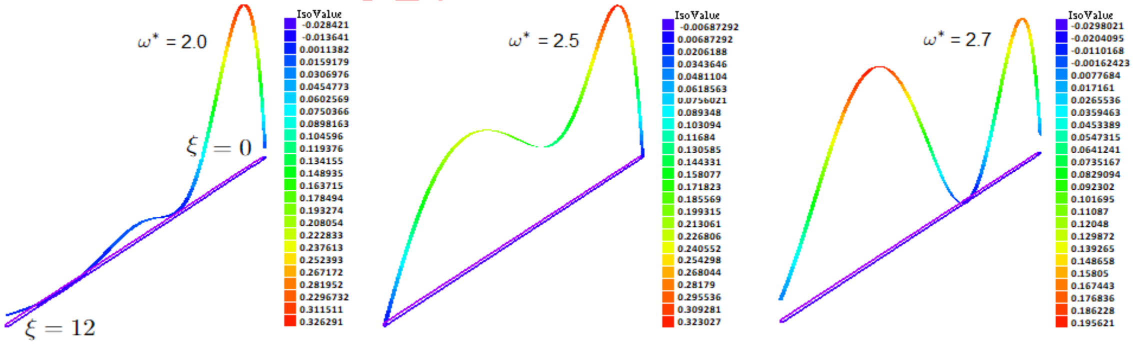

FIGURE 5. Microrotation velocity profiles for varying values of the MMR parameter. Other values of the physical parameters assumed are: $A = -0.5$, $K = 0.5$, $\beta = 0.5$, $M = 0.1$, $\omega = -0.5$, $Pr = 0.3$, $Ec = 0.1$ and $R_m = 1$.

with the variation of relaxation magnetization factor R_m. The relaxation magnetization factor describes the process by which a material's magnetization restores equilibrium after being altered by an external magnetic field. The thermal conductivity of the material will determine the resulting temperature profile. The efficiency of energy transfer during relaxation can depend on temperature. At higher temperatures, the relaxation times may decrease, leading to faster energy dissipation into the medium and a quicker rise in temperature. The MMR parameter is studied in Figure 5 for the microrotation velocity boundary layer. MMR parameter depicts the small-scale rotational or microrotation effects that are impacted by a magnetic field. The observed patterns in the boundary layer profile thicknesses can be affected by various factors, such as fluid's characteristics, the geometry of the flow, and the strength of the magnetic field. The microrotation velocity profiles show an asymmetric trend near and far from the stretching surface. The parameter β impacts on the fluid's macroscopic flow and thermal characteristics and its microstructural features can be seen on the development of boundary layer in Figure 6 and Figure 7, respectively. In these Figures, the influence of β on translational velocity and temperature profiles is observed. It can be seen that the translational velocity and

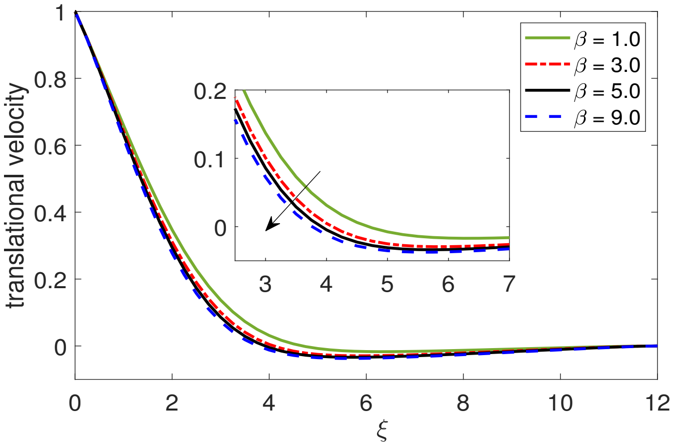

FIGURE 6. Translational velocity profiles for varying values of β. Other values of the physical parameters used are: $A = -0.5$, $K = 1.79$, $\beta = 9.0$, $M = 0.1$, $\omega = 0.5$, $\omega^* = 5.5$, $Pr = 0.3$, $Ec = 0.1$ and $R_m = 3$.

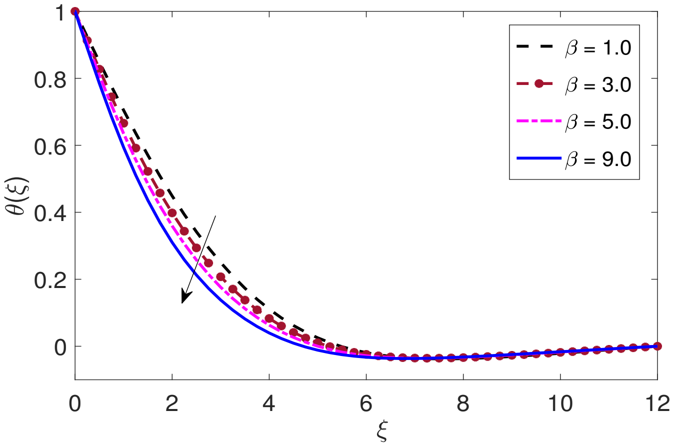

FIGURE 7. Temperature profiles for varying values of β. Other values of the physical parameters used are: $A = -0.5$, $K = 1.79$, $\beta = 9$, $M = 0.1$, $\omega = 0.5$, $\omega^* = 5.5$, $Pr = 0.3$, $Ec = 0.1$ and $R_m = 3$.

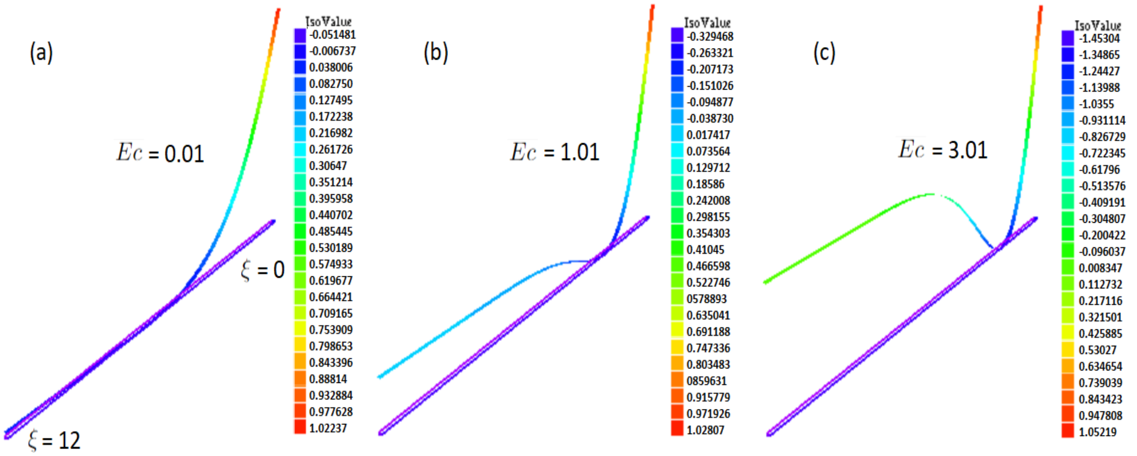

FIGURE 8. Temperature profiles for varying values of Ec. Other values of the physical parameters used are: $A = -0.5$, $K = 1.5$, $\beta = 9$, $M = 0.1$, $\omega = 0.5$, $\omega^* = 5.5$, $Pr = 0.3$ and $R_m = 3$.

temperature profiles will decrease with rising values of the viscosity ratio parameter β. The Eckert number illustrates the relation especially with compressible flow between the kinetic energy and enthalpy, or heat energy of a flowing fluid. The Eckert number and the temperature profile of the system are directly correlated since it considers the difference in temperature between the two points. When a system's Eckert number is high, the fluid's thermal energy and kinetic energy are equal, leading the temperature profile to vary significantly. A fluid with a high Eckert number maintains more kinetic energy than thermal energy. This usually happens in rapid flows. Sharp gradients can be seen in the temperature profile, especially in areas that are rapidly growing or compressing. Figure 8 demonstrates the impact of Eckert number on the temperature profile. Increased values of Eckert number leads to the increase in the thermal boundary layer thickness. In Figure 9, the impact of MMR is observed on temperature profiles. It is seen that rising the values of MMR parameter results in increasing the thermal boundary layer thickness. The values of magnetization parameter A seems to describe the effect of magnetic fields and magnetization dynamics on the fluid behavior. In Figures 10 and 11, an increase in the boundary layer thickness can be seen in case of translational and microrotational velocity profiles by increasing value of the MMR factor. Figure 12 illustrates the translational velocity profiles for different values of the MMR parameter. The influence of MMR on the developed boundary layer profile thickness is examined. In this analysis the MMR parameter is considered with different magnitudes of magnetization. It can be readily seen that the translational velocity boundary layer profiles are lower as magnetization grows. This is caused by the magnetic field's effect on the behavior of the micropolar fluid, which affects the fluid's particle rotations near the stretching surface. Figure 13 shows the microrotational velocity profile for different values of the MMR parameter. It can be observed that with the increasing values of the MMR parameter the boundary layer thickness of the microrotational velocity boundary layer thickness is decreasing. The MMR parameter also plays an important role in the thermal boundary layer thickness development. It can be seen in Figure 14 that the thermal profile increases with increasing values of the MMR parameter. This is highly due to the energy dissipation mechanisms associated with translational and rotational motions in the presence of a magnetic field affects the temperature profile. The interplay between the magnetic field and microrotation may have an impact on the fluid's heat distribution. It is observed that the temperature profile may exhibit greater gradients in regions with significant MMR effect.

5. CONCLUSION

This research presents a novel MMR thermal model with calculations utilizing FreeFEM++ in-house finite element code. First, a thermal boundary layer flow model is developed by considering the theory of magnetorotation within the framework of the micropolar continuum. Second, for the first time in the literature, the developed model is then put into practice using open source code. Previously, no such example is present in the literature of boundary layer

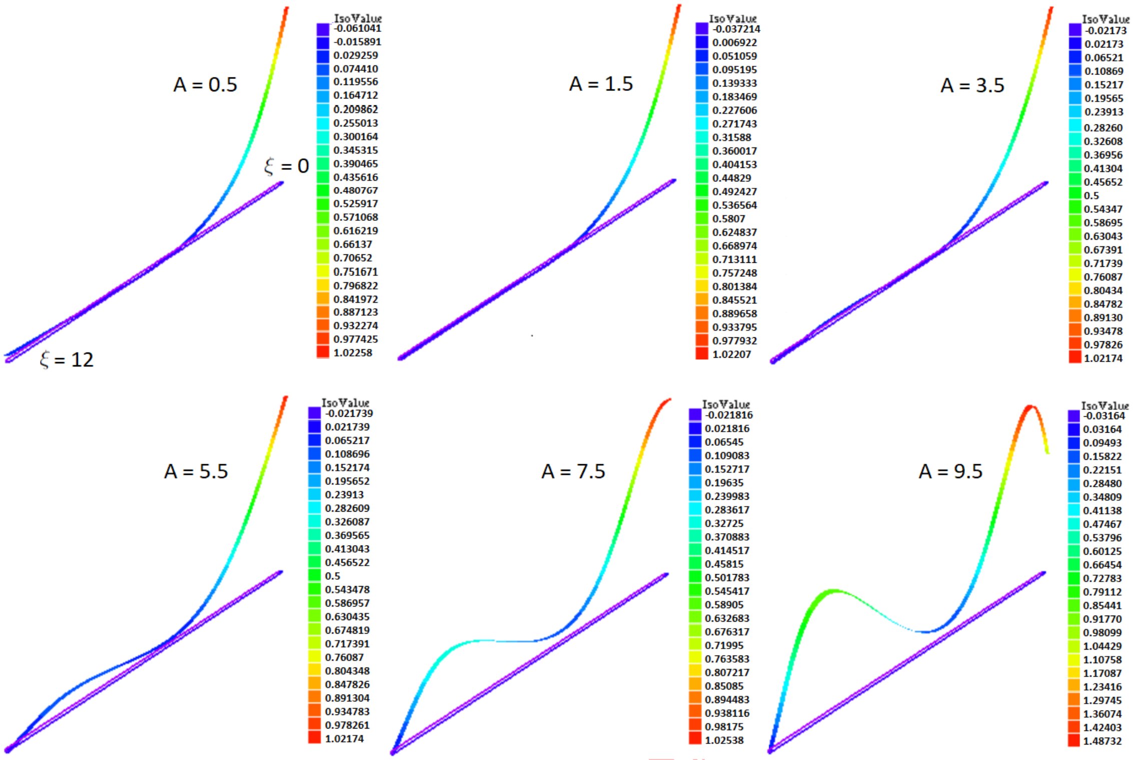

FIGURE 9. Temperature profiles for varying values of A. Other values of the physical parameters used are: $K = 1.5$, $\beta = 1$, $M = 0.1$, $\omega = 0.5$, $\omega^* = 5.5$, $Pr = 0.3$, $Ec = 1.01$ and $R_m = 3$.

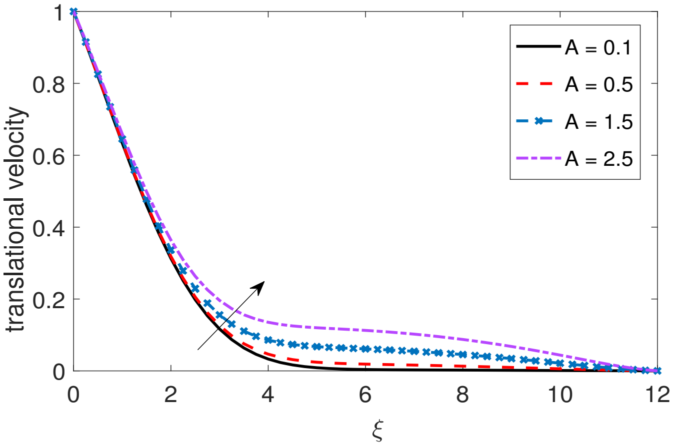

FIGURE 10. Translational velocity profiles for varying values of A. Other values of the physical parameters used are: $K = 1.5$, $\beta = 1$, $M = 0.1$, $\omega = 0.5$, $\omega^* = 5.5$, $Pr = 0.3$, $Ec = 1.01$ and $R_m = 3$.

flows which is calculated through FreeFEM++. It should be noted that FreeFEM++ lacks the built-in functionality to manage one-dimensional simulations. In this instance, though, we successfully used FreeFEM++ to implement the given one-dimensional model. The properties of thermal flow are reviewed when MMR effects are present. This study

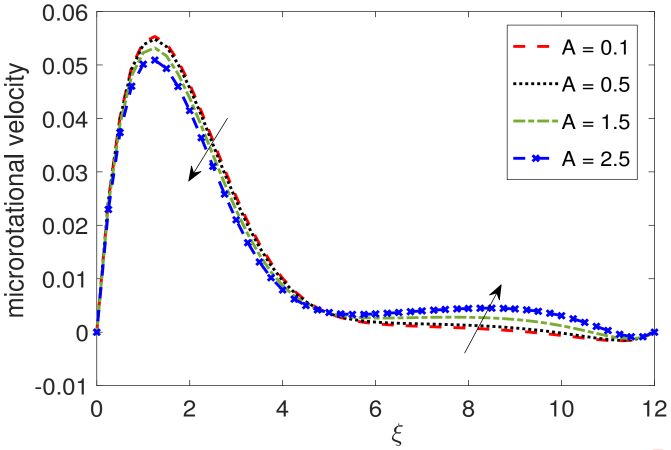

Figure 11. Rotational velocity profiles for varying values of A. Other values of the physical parameters used are: $K = 1.5$, $\beta = 1$, $M = 0.1$, $\omega = 0.5$, $\omega^* = 5.5$, $Pr = 0.3$, $Ec = 1.01$ and $R_m = 3$.

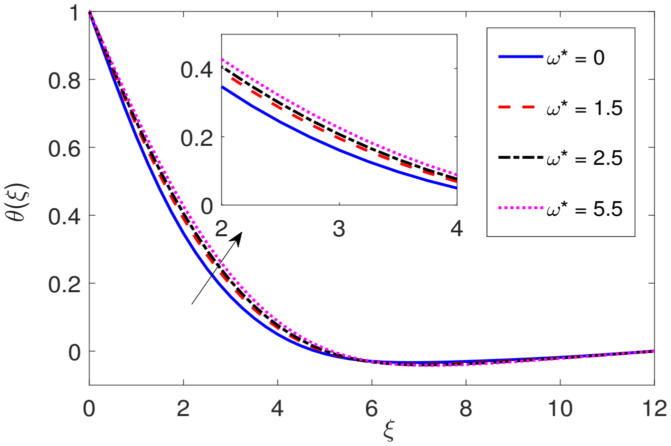

Figure 12. Translational velocity profiles for varying values of $\omega*$. Other values of the physical parameters used are: $A = 1.5$, $K = 1.5$, $\beta = 1$, $M = 0.1$, $\omega = 0.5$, $Pr = 0.3$, $Ec = 0.1$ and $R_m = 3$.

is unique because it uses principles to derive the energy equation that include the MMR effect. The results obtained are discussed in relation to the relevant physical parameters, such as the Nusselt number and skin-friction coefficient with MMR effects. Some of the salient features of the flow observed in the presence of MMR are:

- The skin-friction coefficient increases with an increase in the magnitude of the MMR parameter.
- Increase in the relaxation magnetization factor leads to an increase in the Nusselt number.
- Relaxation magnetization factor R_m affects the thermal boundary layer thickness and it get increased with increasing values of the magnetization.
- Microrotation velocity profiles shows an asymmetric trend near and far from the stretching surface with increasing value of MMR parameter.
- Increasing value of MMR leads to turbulent thermal boundary layer development. The development of vortices can be observed as the sub-boundary thermal layer are developed with increasing values of MMR parameter.
- Translational boundary layer thicknesses are increased with increasing values of MMR.

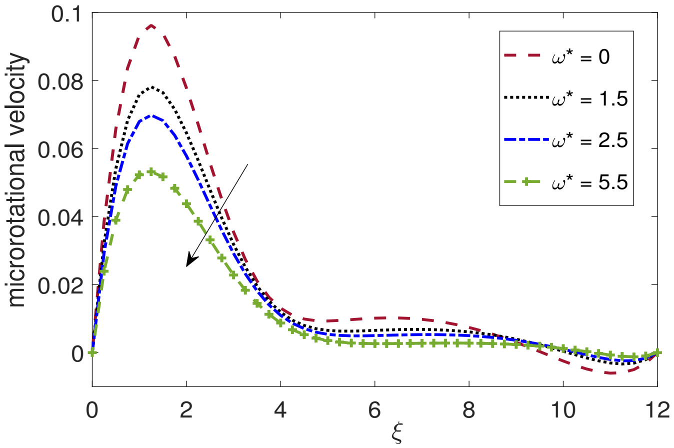

FIGURE 13. Rotational velocity profiles for varying values of $\omega*$. Other values of the physical parameters used are: $A = 1.5$, $K = 1.5$, $\beta = 1$, $M = 0.1$, $\omega = 0.5$,Pr $= 0.3$, $Ec = 0.1$ and $R_m = 3$.

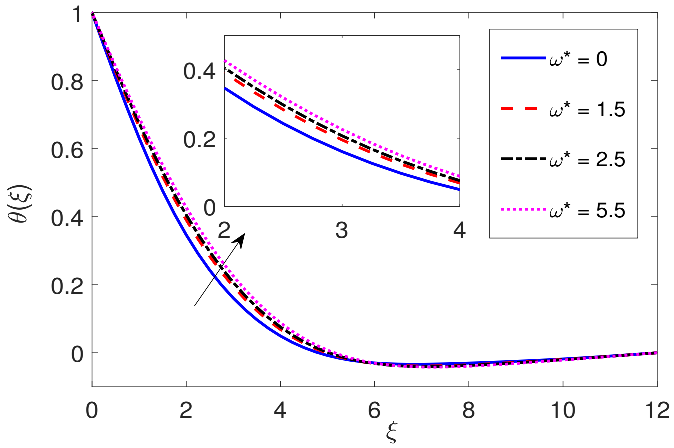

FIGURE 14. Temperature profiles for varying values of $\omega*$. Other values of the physical parameters used are: $A = 1.5$, $K = 1.5$, $\beta = 1$, $M = 0.1$, $\omega = 0.5$, $Pr = 0.3$, $Ec = 0.1$ and $R_m = 3$.

- The microrotational velocity profiles thicknesses are decreasing near the stretching surface and increasing away from the stretching surface with an increasing values of MMR.

The present analysis has potential applications in various industrial and biomedical processes where control of heat and fluid transport under magnetic fields is essential. For instance, MMR effects in micropolar fluids are relevant to bioengineering applications such as targeted drug delivery, magnetic hypothermia, and lab-on-chip microfluidic systems. Similarly, in industrial processes like chemical transport, cooling of microelectronic devices, and metallurgical operations, the findings provide valuable insights into improving heat transfer and flow control under magnetohydrodynamics conditions.

The proposed FreeFEM++ based finite element framework demonstrates high flexibility and accuracy for solving complex magneto-thermal micropolar flow problems incorporating MMR effects. However, several numerical and computational limitations must be acknowledged. First, the method is computationally intensive for highly refined meshes and extreme parameter regimes, requiring significant processing time. Second, the numerical stability and convergence of the FreeFEM++ solver are sensitive to mesh design, element order, and solver tolerances, necessitating careful parameter tuning. Third, while FreeFEM++ supports three-dimensional simulations, the current implementation focuses on a two-dimensional formulation; extending the analysis to three-dimensional geometries would demand additional stabilization techniques and computational resources. Finally, for highly nonlinear coupled systems, advanced features such as mesh adaptivity or hybrid solvers may be required to maintain solution stability. Future extensions of this work will aim to overcome these limitations and enhance the scalability of the proposed framework.

REFERENCES

[1] A. Abd-Alla, S. Abo-Dahab, E. N. Thabet, and M. Abdelhafez, *Heat and mass transfer for MHD peristaltic flow in a micropolar nanofluid: mathematical model with thermophysical features*, Scientific Reports, *12*(1) (2022), 21540.

[2] B. Ali, S. A. Khan, A. K. Hussein, T. Thumma, and S. Hussain, *Hybrid nanofluids: Significance of gravity modulation, heat source/sink, and magnetohydrodynamic on dynamics of micropolar fluid over an inclined surface via finite element simulation*, Applied Mathematics and Computation, *419* (2022), 126878.

[3] K. E. Aslani, and I. E. Sarris, *Effect of micromagnetorotation on magnetohydrodynamic Poiseuille micropolar flow: Analytical solutions and stability analysis*, Journal of Fluid Mechanics, *920*(A25) (2021).

[4] K. E. Aslani, L. Benos, E. Tzirtzilakis, and I. E. Sarris,*Micromagnetorotation of MHD micropolar flows*, Symmetry, *12*(1) (2020), 148–160.

[5] K. E. Aslani and I. E. Sarris, *Effect of micromagnetorotation on magnetohydrodynamic Poiseuille micropolar flow: Analytical solutions and stability analysis*, J. Fluid Mech., *920*(A25) (2021).

[6] K. E. Aslani, and I. E. Sarris, *Effect of micromagnetorotation on the heat transfer of micropolar Hartmann flow*, Thermal Science and Engineering Progress, *26* (2021), 101129.

[7] E. Cosserat, and F. Cosserat, *Theories des corps deformables*, Nature, *81* (1909), 67.

[8] A. Divya, S. R. Sheri, and A. K. Suram, *Finite element analysis of MHD naturally convective flow past an exponentially accelerated plate with viscous dissipation*, Numerical Heat Transfer, Part B: Fundamentals, *85*(9) (2024), 1115–1129.

[9] A. C. Eringen, *Theory of micropolar fluids*, Journal of Mathematics and Mechanics, *146* (2020), 821–831.

[10] D. Gupta, L. Kumar, A.O. Bég, and B. Singh, *Finite element analysis of MHD flow of micropolar fluid over a shrinking sheet with a convective surface boundary condition*, Journal of Engineering Thermophysics, *27* (2018), 202–220.

[11] I. Hameed and M. S. Khan, *On the simulations of micromagnetorotation (MMR) effects within micropolar conducting liquids*, International Journal of Ambient Energy, *45*(1) (2024), 2318627.

[12] F. Hecht, *New development in FreeFem++*, J. Numer. Math., *20*(3-4) (2012), 251–265.

[13] M. S. Khan, M. A. Memon, I. Khan, and S. M. Eldin, *Finite element based direct and iterative approach to investigate a magneto-micropolar flow through a rectangular channel*, Alexandria Engineering Journal, *75* (2023), 55–66.

[14] M. S. Khan and I. Hameed, *FreeFEM++ based heat transfer analysis of an electrically induced magnetic flow within the framework of micropolar continuum*, Numerical Heat Transfer, Part A: Applications, (2023). 1–19.

[15] M. S. Khan, I. Hameed, M. A. Memon, and E. Bonyah, *Computational analysis of magnetic induced micropolar flow in a rectangular channel through FreeFem++*, AIP Advances, *13*(4) (2023).

[16] J. Kierzenka and L. F. Shampine, *A BVP solver based on residual control and the MATLAB PSE*, ACM Transactions on Mathematical Software, *27*(3) (2001), 299–316.

[17] M. Lajvardi, J. M. Rad, I. Hadi, A. Gavili, T. D. Isfahani, F. Zabihi, and J. Sabbaghzadeh, *Experimental investigation for enhanced ferrofluid heat transfer under magnetic field effect*, Journal of Magnetism and Magnetic Materials, *322* (21) (2010), 3508–3513.

[18] J. S. Mehta, R. Kumar, H. Kumar, and H. Garg, *Numerical Investigation and Comparison of Thermal Performance of Ferrofluid in Different Closed Loop Configurations*, Journal of Physics: Conference Series, *1240*(1) (2019), 012056.

[19] A. Mishra and M. Kumar, *Viscous dissipation and Joule heating influences past a stretching sheet in a porous medium with thermal radiation saturated by silver–water and copper–water nanofluids*, Special Topics & Reviews in Porous Media: An International Journal, *10*(2) (2019).

[20] H. Schlichting and K. Gersten, *Boundary-Layer Theory*, Springer, *9* (2016).

[21] M. Shamshuddin and T. Thumma, *Numerical study of a dissipative micropolar fluid flow past an inclined porous plate with heat source/sink*, Propulsion and Power Research, *8*(1) (2019), 56–68.

[22] M. Shamshuddin, O. A. Bég, M. S. Ram, and A. Kadir, *Finite element computation of multi-physical micropolar transport phenomena from an inclined moving plate in porous media*, Indian Journal of Physics, *92*(2) (2018), 215–230.

[23] P. R. Sharma, S. R. Mishra, P. K. Pattnaik, S. Tinker, and R. Allipudi, *Numerical study of slip flow of a micropolar fluid through a porous wedge surface with the impact of a chemical reaction and heat source/sink*, International Journal of Modern Physics B, *38*(23) (2024), 2450314.

[24] S. Sharma, V. Lambha, S. Mittal and R. Verma, Journal of Engineering Tribology, *237*(7) (2023), 1461-1470.

[25] S. R. Sheri and M. Shamshuddin, *Finite element analysis on transient magnetohydrodynamic (MHD) free convective chemically reacting micropolar fluid flow past a vertical porous plate with Hall current and viscous dissipation*, Propulsion and Power Research, *7*(4) (2018), 353–365.

[26] K. Shizawa and T. Tanahashi, *New constitutive equations for conducting magnetic fluids with internal rotation: thermodynamical discussions*, Bull. JSME, *29* (1986) , 2878—2884.

[27] K. Shizawa and T. Tanahashi, *New constitutive equations for conducting magnetic fluids with internal rotation: thermodynamical discussions*, Bulletin of JSME, *29*(255) (1986), 2878–2884.

[28] C. Yuan, H. N. Zhang, Y. K. Li, X. B. Li, J. Wu, and F. C. Li, *Nonlinear effects of viscoelastic fluid flows and applications in microfluidics: A review*, Proceedings of the Institution of Mechanical Engineers, Part C: Journal of Mechanical Engineering Science, *234*(22) (2020), 4390–4414.